Supplementary Material

Title: Tsunamigenic earthquake simulations using experimentally derived friction laws

S. Murphy[1,2*], G. Di Toro[3,4], F. Romano[1], A. Scala[1], S. Lorito[1], E. Spagnuolo[1], S. Aretusini[3], G. Festa[4], A. Piatanesi[1], S. Nielsen[5]

[1]Istituto Nazionale di Geofisica e Vulcanologia, Rome, Italy

[2]Ifremer, Plouzané, France

[3]University of Manchester, Manchester, United Kingdom

[4]Università degli Studi di Padova, Padua, Italy

[5]Università di Napoli Federico II, Naples, Italy

[6]Durham University, Durham United Kingdom

*shane.murphy@ifremer.fr

A1. Model Setup

	ρ (kg/m^3)	v_p (km/s)	v_s (km/s)	Colour in Fig. 1
Oceanic Mantle	3300	8.0	4.6	Purple
Oceanic	3000	7.3	4.4	Yellow
Lower Crust	3000	8.0	4.6	Blue
Middle Crust	2800	7.1	4.1	Red
Wedge	2500	4.7	2.1	Green
Continental / upper crust	2500	6.2	3.6	Gold
Oceanic Surface	2800	7.1	4.4	Brown

Table S1: Elastic parameters used in numerical model as depicted in Fig. 1 (main text).

No. of nodes per element face	9
dt	$1\ 10^{-3}$ s
Average element length along fault	2.47 km
Largest Courant No.	$6\ 10^{-3}$

Table S2: Numerical model parameters.

	Clay-like	Rock-like
μ_s	0.25	0.7
μ_d	0.1	0.2
α	3.7	78
β	1	1

Table S3: Frictional properties used for clay-like and rock-like materials. Rock-like frictional parameters are based on Del Gaudio et al.(2009) for peridotite (note that similar values are valid for gabbro, basalts and serpentinites, the most common rocks of the oceanic lithosphere). The thermal slip weakening friction law produces a similar evolution of stress with slip and roughly similar thermal weakening distances observed in thermal pressurization modelling for the Japanese trench(Hirono et al., 2016). See Methods for the clay-like materials frictional properties.

Run	V	σ_n	d_{th}	Ref.
	(m/s)	MPa	(m)	
HVR784	1.04	0.28	16.76	(Brantut et al., 2008)
HVR787	1.04	0.48	6.01	(Brantut et al., 2008)
HVR782	1.04	0.59	5.54	(Brantut et al., 2008)
HVR786	1.04	0.82	6.84	(Brantut et al., 2008)
HVR781	1.04	0.99	6.34	(Brantut et al., 2008)
HVR788	1.04	1.15	4.37	(Brantut et al., 2008)
HVR780	1.04	1.32	1.37	(Brantut et al., 2008)
HVR754	1.04	0.6	4.17	(Brantut et al., 2008)
HVR905	1.04	0.62	2.10	(Brantut et al., 2008)
1372	1.31	1	3.00	(Ferri et al., 2011)
1868	1.31	1	2.50	(Ferri et al., 2011)
405	1.3	9	0.06	(Bullock et al., 2015)
395	1.3	9	0.07	(Bullock et al., 2015)
820	1	4	0.07	(Proctor et al., 2014)
821	1	11.8	0.09	(Proctor et al., 2014)
822	1	17.8	0.06	(Proctor et al., 2014)
823	1.1	22.4	0.05	(Proctor et al., 2014)
745	1.2	8.3	0.08	(Proctor et al., 2014)
HVR178	1.03	0.66	7.50	(Mizoguchi et al., 2009)
HVR189	1.03	0.375	7.71	(Mizoguchi et al., 2009)
HVR190	1.03	0.345	11.39	(Mizoguchi et al., 2009)
HVR183	1.03	0.64	12.71	(Mizoguchi et al., 2009)
HVR184	1.03	0.636	8.89	(Mizoguchi et al., 2009)
HVR180	1.03	1.26	1.39	(Mizoguchi et al., 2009)
HVR185	1.03	1.289	2.20	(Mizoguchi et al., 2009)
HVR182	1.03	1.873	2.48	(Mizoguchi et al., 2009)
HVR188	1.03	1.856	1.83	(Mizoguchi et al., 2009)
LHV304	1.4	0.6	8.38	(Yao et al., 2013a)
LHV305	1.4	0.8	4.87	(Yao et al., 2013a)
LHV306	1.4	1	2.56	(Yao et al., 2013a)
LHV308	1.4	1.3	1.73	(Yao et al., 2013a)
LHV307	1.4	1.7	1.35	(Yao et al., 2013a)
LHV309	1.4	2.5	0.78	(Yao et al., 2013a)
LHV242	1.4	0.8	6.04	(Yao et al., 2013b)
LHV241	1.4	0.8	4.14	(Yao et al., 2013b)
LHV243	1.4	0.8	6.64	(Yao et al., 2013b)
LHV244	1.4	0.8	4.61	(Yao et al., 2013b)
LHV248	1.4	0.8	3.81	(Yao et al., 2013b)
LHV246	1.4	0.8	3.47	(Yao et al., 2013b)
LHV256	1.4	0.8	5.84	(Yao et al., 2013b)
LHV251	1.4	0.8	1.97	(Yao et al., 2013b)
LHV253	1.4	0.8	3.34	(Yao et al., 2013b)

LHV365	1.4	0.8	3.14	(Yao et al., 2013b)
HVR1489	1.3	1.01	0.23	(Togo et al., 2011)
HVR1490	1.3	0.8	3.25	(Togo et al., 2011)
HVR1491	1.3	0.61	4.14	(Togo et al., 2011)
HVR1494	1.3	1.21	1.51	(Togo et al., 2011)
HVR1496	1.3	1.64	1.63	(Togo et al., 2011)
HVR1497	1.3	2.05	1.22	(Togo et al., 2011)
HVR1502	1.3	3.04	0.63	(Togo et al., 2011)
s1168	1.3	5	0.18	(Aretusini et al., 2017)
s1167	1.3	5	0.10	(Aretusini et al., 2017)
s1166	1.3	5	0.64	(Aretusini et al., 2017)

Table S4: Source of experimential data plotted in Fig. 3.

Case Study Colour in Fig. 3	Max. shear stress depth (km)	Nucleation depth (km)
Deep	39	34
Intermediate	20	23
Shallow	17	14.5

Table S5: Model name and corresponding depth of maximum initial stress and nucleation.

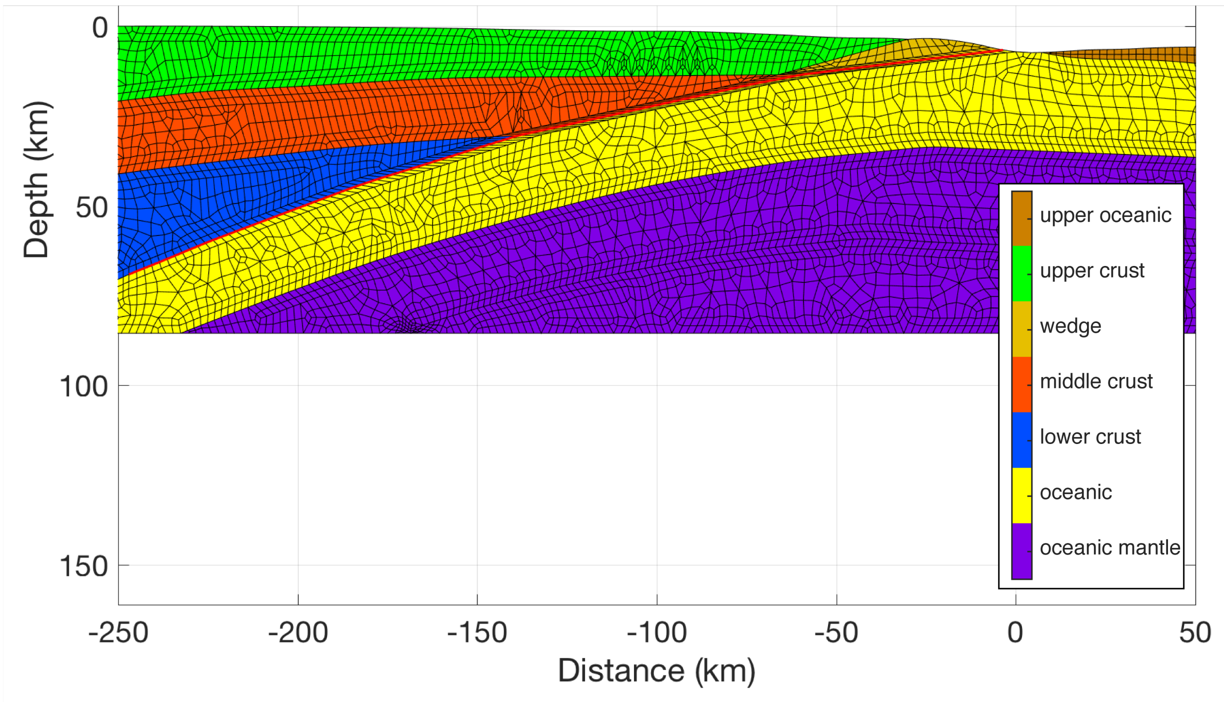

Figure S1: mesh used in simulations where boundary of cell is demarked by solid black line. Solid red line represents the fault. Colour coding of layers is the same as that used in Fig. 2 in main text.

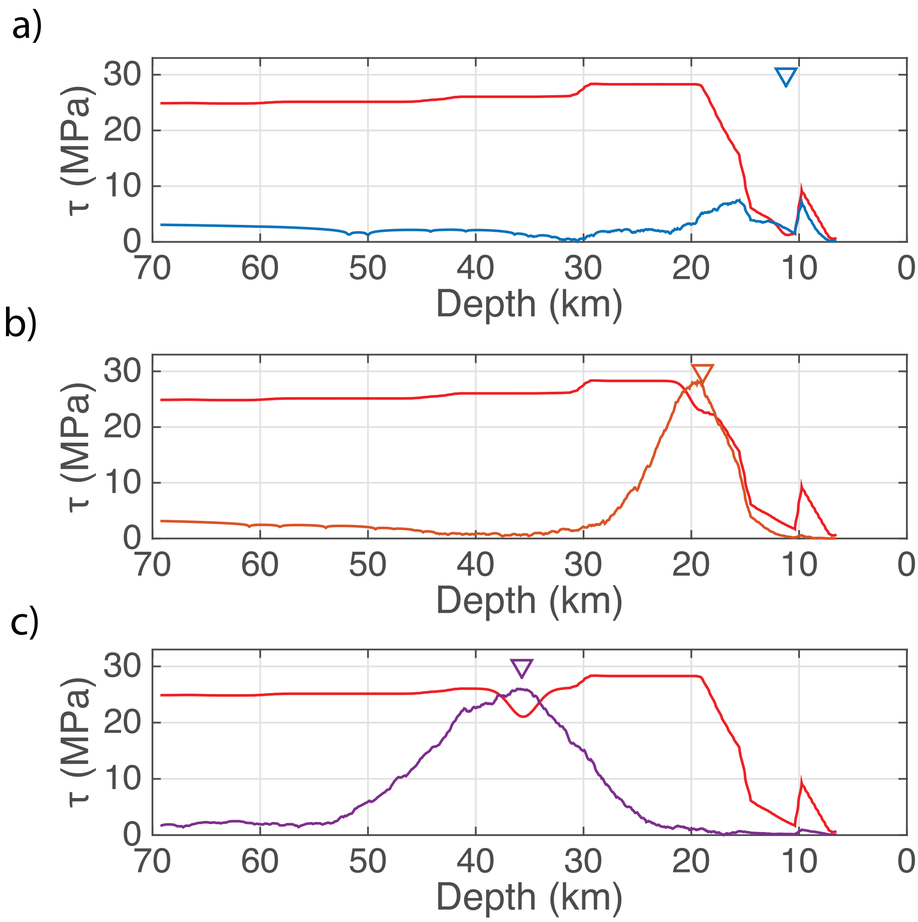

Figure S2: Initial stress (blue, orange, and purple lines) and yield stress (red line) containing nucleation depth (denoted by triangles). **a)** shallow, **b)** intermediate and **c)** deep case study simulations.

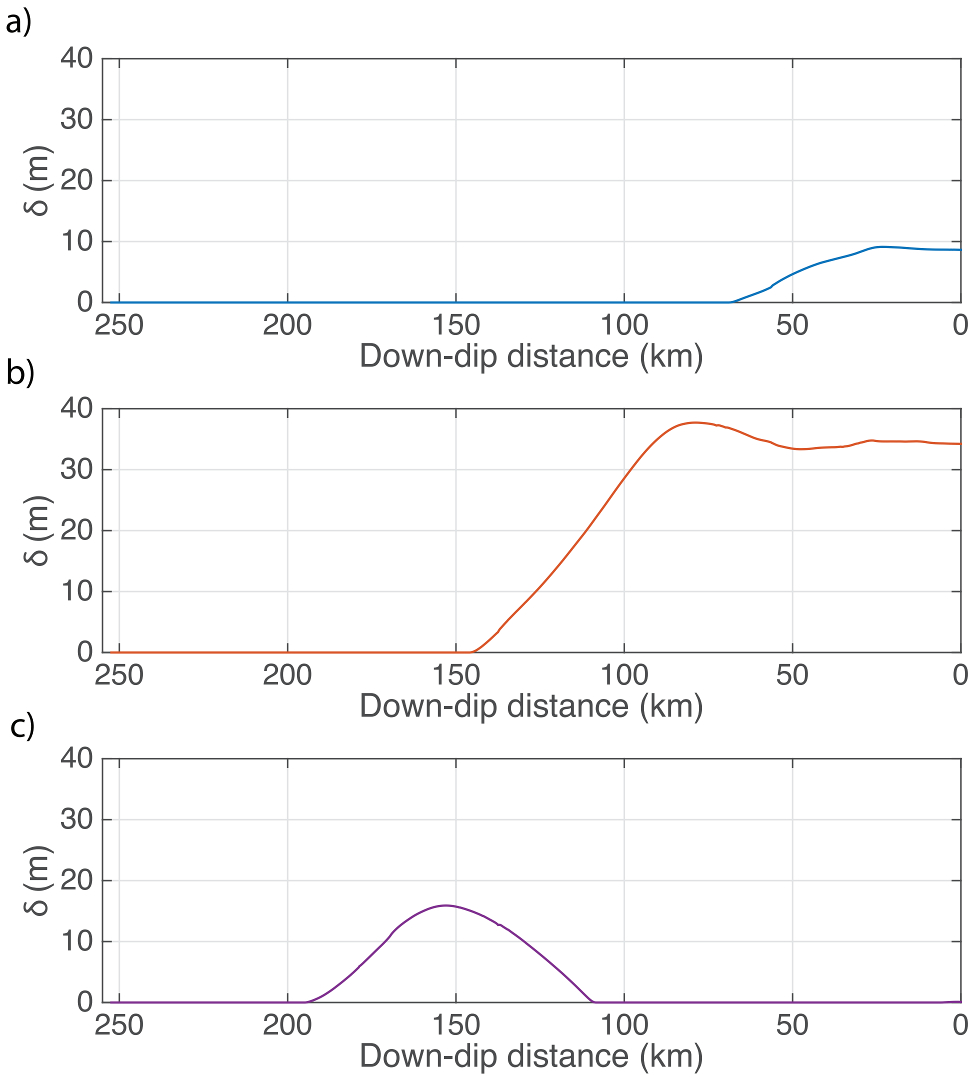

Figure S3: Final slip as a function of fault down-dip distance from the free surface (i.e., seafloor). **a)** shallow, **b)** intermediate and **c)** deep case study simulations (main text Fig. 2).

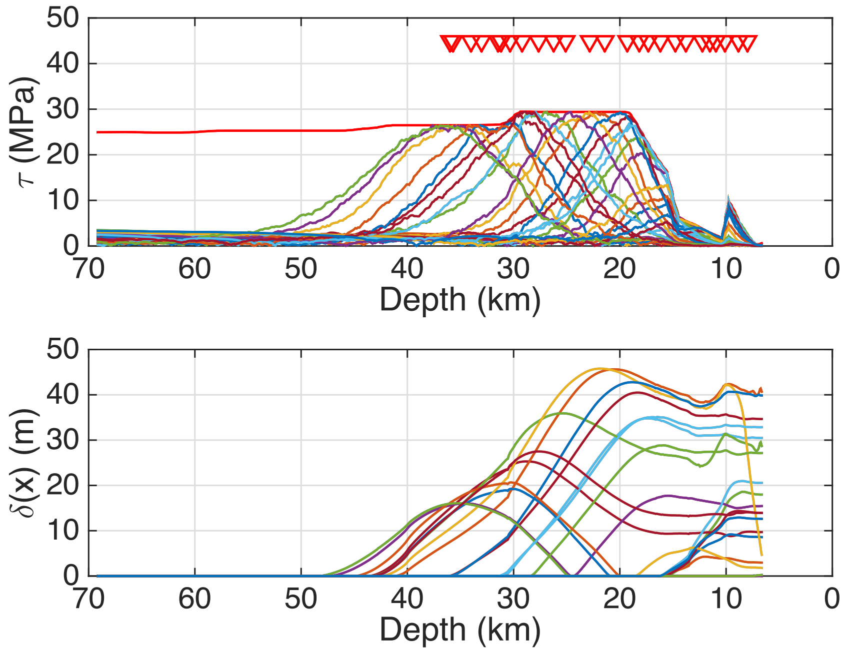

Figure S4: Initial stress (top subplot) and resulting slip distributions (bottom subplot) from the simulations plotted in Fig. 3 in the main text.

A2. Scaling between principal stresses

The shear and normal stress (τ and σ_n respectively) can be defined in terms of the principal stresses σ_1 and σ_2 where $\sigma_1 > \sigma_2$ as (Jaeger et al., 2007):

$$\tau = \frac{-(\sigma_1 + \sigma_2)}{2} \sin 2\theta \qquad \text{(Eqn. S1)}$$

$$\sigma_n = \frac{(\sigma_1 + \sigma_2)}{2} + \frac{(\sigma_1 - \sigma_2)}{2} \cos 2\theta \qquad \text{(Eqn. S2)}$$

θ is the anti-clockwise rotation from the direction of maximum principal stress to the normal of the fault plane which in the case of subduction zones is horizontal, the fault dip ϕ is therefore defined as $\phi = \theta - \pi/2$. Substituting Byleree's Law ($\tau = \mu\, \sigma_n$ where μ is the coefficient of friction) into Eqn S1 to replace τ, this new equation can be combined with Eqn S2 to give:

$$\sigma_1 = \left\{ \frac{\sin(2\,\theta) + \mu\cos(2\,\theta) - \mu}{\mu + \mu\cos(2\,\theta) + \sin(2\,\theta)} \right\} \sigma_2 \qquad \text{(Eqn. S3)}$$

This equation provides a scaling relationship between the principal stress components based on the coefficient of friction and (indirectly) the fault dip. In our numerical model the static coefficient of friction varies from 0.25 at the surface to 0.7 at depth, similarly the fault geometry varies by a large amount. In the literature, Ma et al. (2012) (referenced in the manuscript) applied a value $\sigma_1 = 4.7545\, \sigma_2$ for subduction zone fault while Brace and Kohlstedt (1980) used a ratio of $\sigma_1 = 5\, \sigma_2$ in order to estimate a general estimate of lithospheric stress. We have taken a ratio of 4.05 which corresponds to fault dipping at 37° with a coefficient of friction of 0.7. It is also valid for a 10.6° fault dip with a coefficient of friction of 0.5.

A3. Tsunami Source

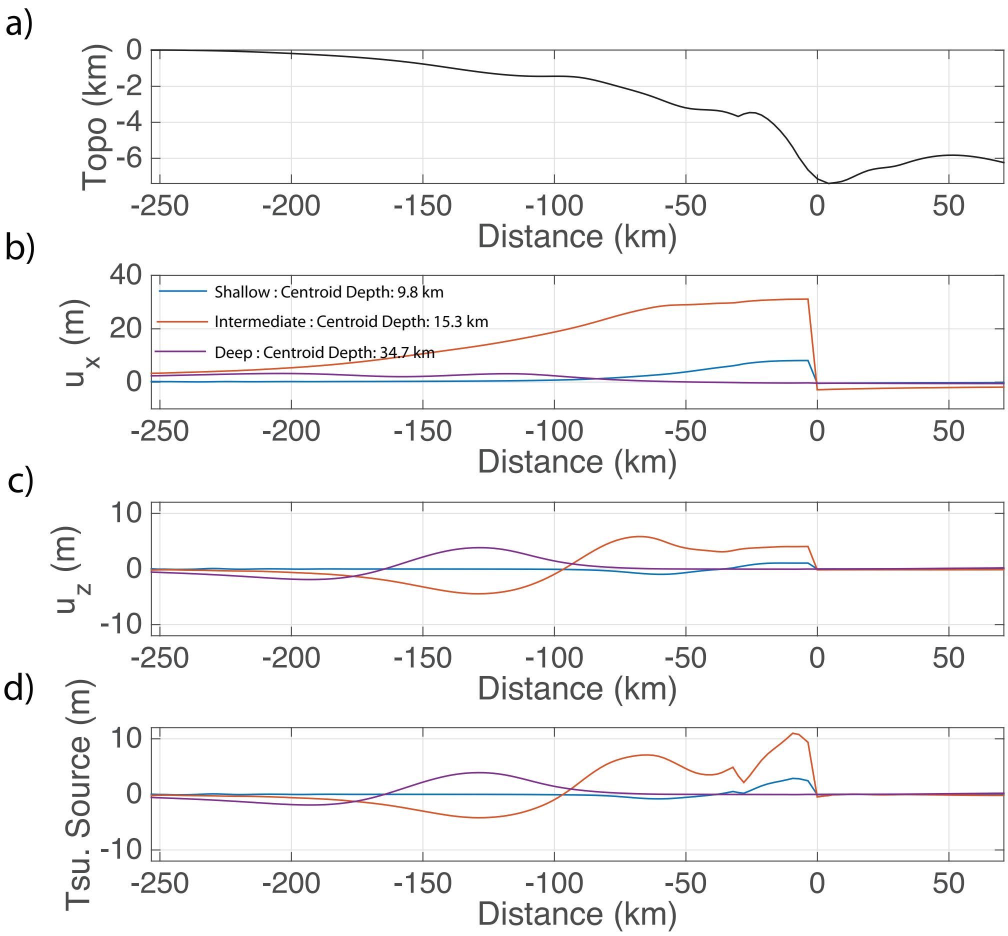

Figure S5: The displacement used for a tsunami source is based on the vertical seafloor displacement and the horizontal motion of the trench slope. It is calculated using the formula $d = u_z + \frac{\partial T}{\partial x} u_x$ where u_z and u_x and the vertical and horizontal seafloor displacements respectively and $\frac{\partial T}{\partial x}$ is the gradient of the water depth (Tanioka and Satake, 1996). **a)** is the seafloor depth in the numerical model, **b)** is the horizontal displacement in the three case study simulations, **c)** is the vertical seafloor displacement, and **d)** is the displacement accounted for in a tsunami source.

A4. Calculation for 1-Dimensional normalised rupture duration and seismic moment

The normalised rupture duration is calculated in a similar manner to previous work (Houston et al., 1998) however the change from a 2-D fault to a 1-D line fault needs to be accounted for. In the case of this work the moment M_o for a 1-D line is defined as:

$$M_o = G\, W\, \bar{\delta} \qquad \text{(Eqn. S4)}$$

where G the shear modulus, W the fault rupture width and $\bar{\delta}$ the average slip(Mitsui and Yagi, 2013). The average slip can also be defined in terms of the average static stress drop, $\Delta\sigma$:

$$\bar{\delta} = \mathrm{C}\frac{\Delta\sigma}{G}L \qquad \text{(Eqn. S5)}$$

where C is a constant and L is the rupture length. Setting the L equal to W, and substituting it in terms of rupture duration (i.e., $W = T\, v_r$, where T is rupture duration and v_r is rupture velocity). Combining Equations S1, S2 and substituting in the duration in place of the width produces:

$$T = \frac{1}{v_r}\sqrt{\frac{M_o}{\mathrm{C}\,\Delta\sigma}} \qquad \text{(Eqn. S6)}$$

This is different for the 2-D case (i.e., $T \propto {M_o}^{1/3}$). Therefore, normalising the 1-D duration to a given reference moment, M_o^{ref}, is defined as:

$$T_N^{1D} = T\left(\frac{M_o}{M_o^{ref}}\right)^{1/2} \qquad \text{(Eqn. S7)}$$

For the normalised duration for observations (Bilek and Lay, 1999) M_o^{ref} was set to a magnitude 6 event. To make our numerical results comparable to these observations, we calculated the slip distribution of a circular asperity of M 6 and calculated the moment along a line through the centre of the asperity. This gave a value of 3.7 10^{14} Pa m^2 which M_o^{ref} was set equal to in Eqn. S7.

A5. Sensitivity Analysis: depth at which fluid retention depth occurs

Two additional ensembles were run where the fluid retention depth, z_{FRD}, was shifted ± 5km of the original depth, that is depths of 7 km and 17 km. The effect on yield stress and initial stress distributions, is depicted in Fig. S6 for z_{FRD} = 7 km, and in Fig. S7 for z_{FRD} = 17 km. In both cases 15 simulations were performed. Fig. S8 shows the comparison between the three ensembles in terms of moment, average static stress drop, normalised rupture duration, average breakdown energy, average slip-rate per earthquake and average rupture velocity. Fig. S8 shows that the earthquakes in the ensemble with z_{FRD} = 17 km are similar to case in the main text (i.e., z_{FRD} = 12 km), however the depth dependent trends are different in the case with z_{FRD} = 7 km.

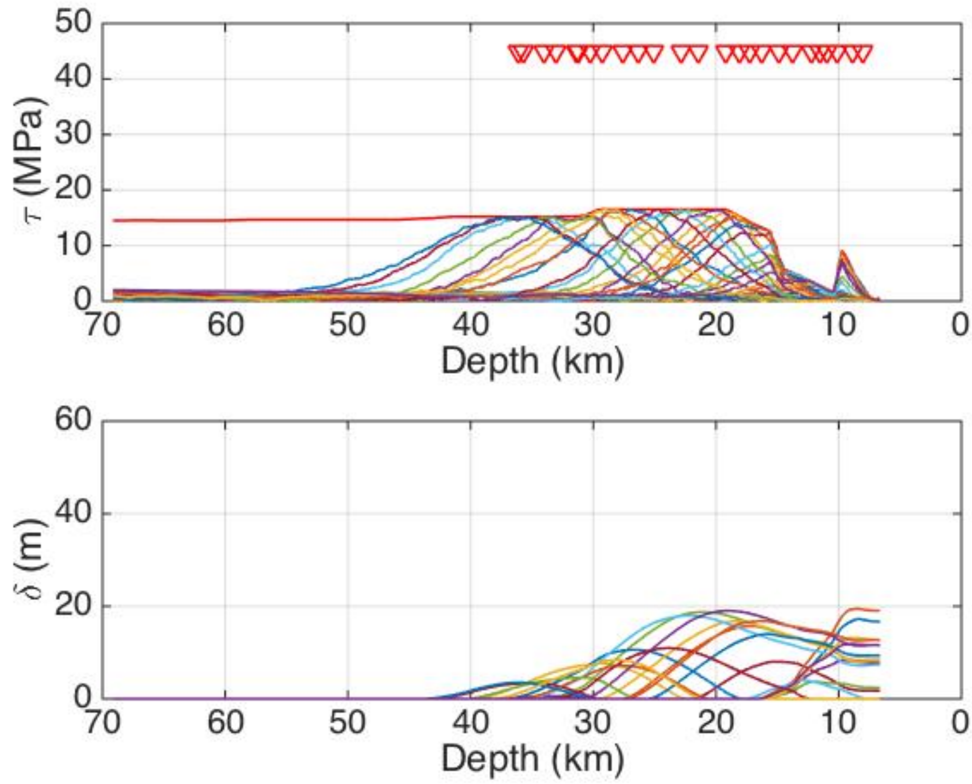

Figure S6: Initial stress (top subplot) and resulting slip distributions (bottom subplot) in the z_{FRD} = 7 km case. In the top subplot the red line is the yield stress and each coloured line is an initial stress distribution used in an individual simulation. The green triangles denote the location of seismic rupture nucleation. In the bottom subplot the colour code of the slip distributions match colour code used for the initial stress distributions used in the subplot above.

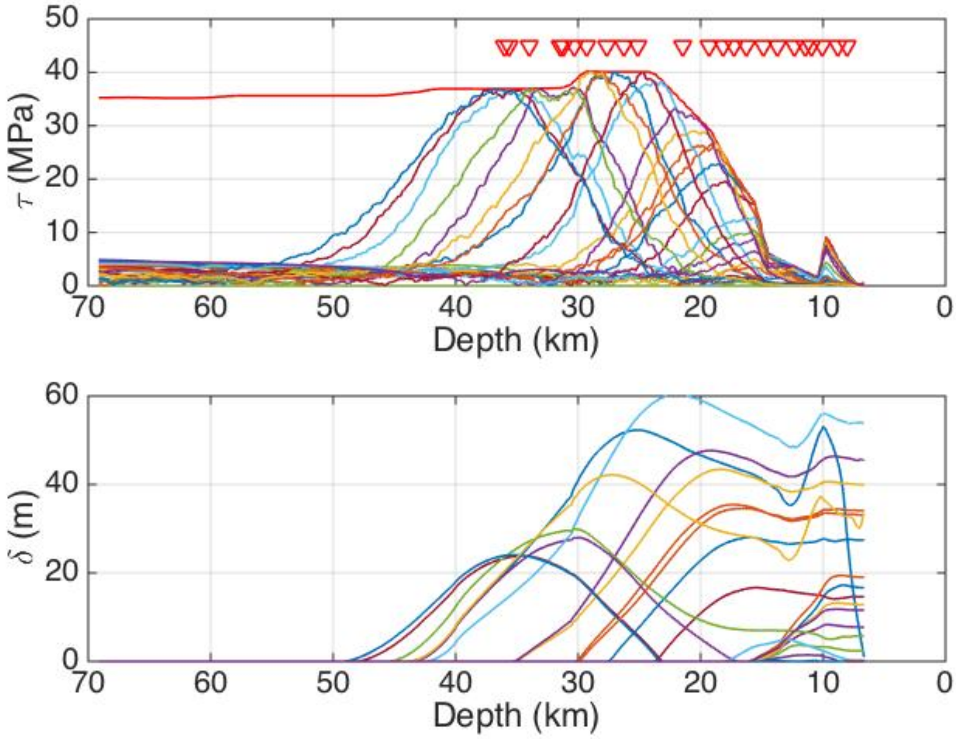

Figure S7: Initial stress (top subplot) and resulting slip distributions (bottom subplot) in the z_{FRD} = 17 km case. In the top subplot the red line is the yield stress and each coloured line is an initial stress distribution used in an individual simulation. The green triangles denote the location of the seismic rupture nucleation. In the bottom subplot the colour code of the slip distributions match colour code used for the initial stress distributions used in the subplot above.

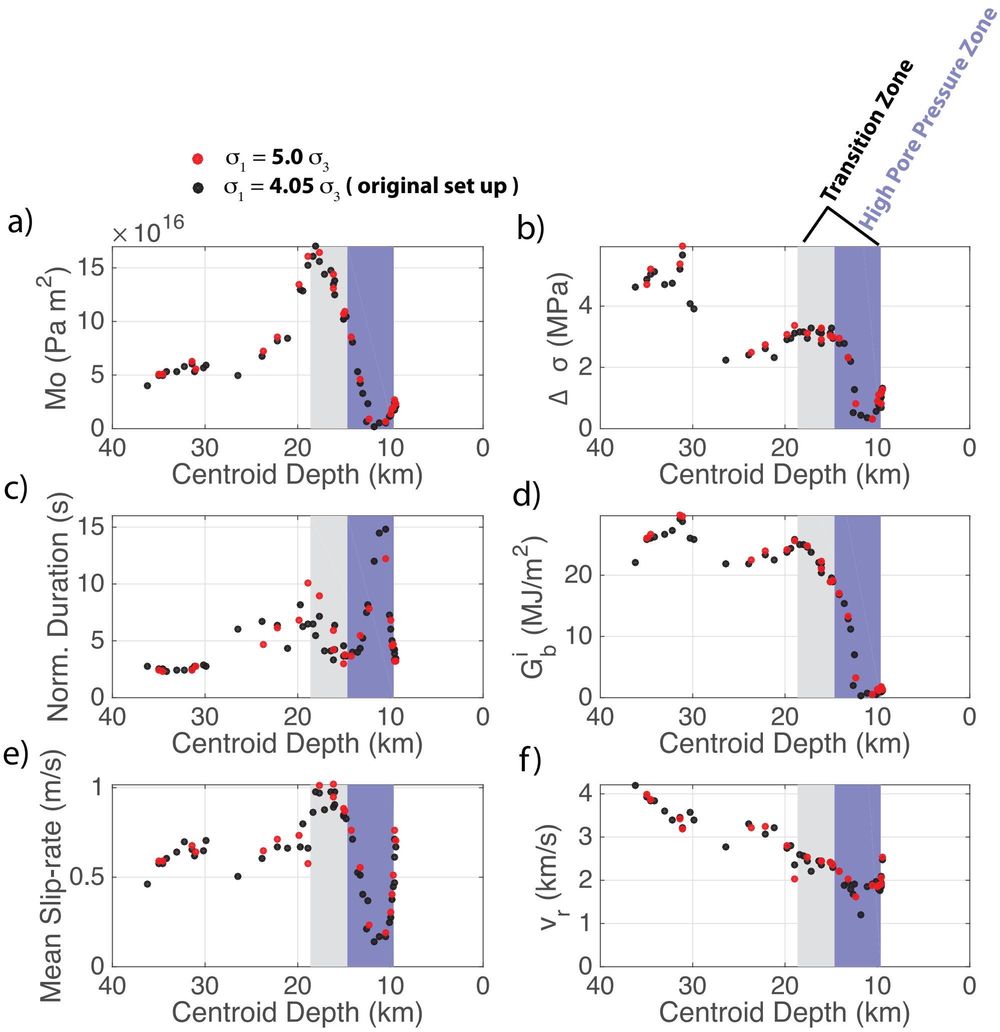

Figure S8: Testing the effect of changing the relationship between the principal components of stress. Black dots are for the simulations as described in the main text, that is $\sigma_1 = 4.05\,\sigma_3$, while red dots are for $\sigma_1 = 5.0\,\sigma_3$. **a)** Seismic moment of the 1-D line earthquake; a constant $G = 30$ GPa rather than a depth dependent shear modulus was used in the calculation as is commonly used in observational seismology. **b)** Average static stress drop; **c)** normalised rupture duration; **d)** average breakdown energy; **e)** average slip-rate per earthquake and **f)** average rupture velocity.

A6. Averaged rupture features for 3 case studies.

	Shallow	Intermediate	Deep
G_b^i (MJ/m^2)	1.15	19.6	25.8
$\Delta\sigma$ (MPa)	0.96	3.0	4.76
v_r (km/s)	1.7	2.5	3.9
T_r (s)	22.6	31.6	18.6
$\dot{\delta}$ (m/s)	0.24	0.65	0.41

Table S6: Earthquake source parameters for four simulated ruptures reported in Fig. 2 of the main text. Average breakdown energy G_b^i based on the assumed slip weakening friction law (Eq. S1), the numerical integration of stress (Eq. S2) and the average static stress drop. In all cases only points where coseismic slip occurs are considered when calculating the mean breakdown energy and static stress drop. v_r is the average rupture velocity, T_r is the average rise time and $\dot{\delta}$ is the average slip-rate on the fault. All averaged values are based on section of the fault that slips.

References

Bilek, S.L., Lay, T., 1999. Rigidity variations with depth along interplate megathrust faults in subduction zones. Nature 400, 443–446. doi:10.1038/22739

Brace, W.F., Kohlstedt, D.L., 1980. Limits on lithospheric stress imposed by laboratory experiments. Journal of Geophysical Research: Solid Earth (1978–2012) 85, 6248–6252. doi:10.1029/JB085iB11p06248

Brantut, N., Schubnel, A., Rouzaud, J.N., Brunet, F., Shimamoto, T., 2008. High-velocity frictional properties of a clay-bearing fault gouge and implications for earthquake mechanics. Journal of Geophysical Research: Solid Earth (1978–2012) 113, B10401. doi:10.1029/2007JB005551

Bullock, R.J., De Paola, N., Holdsworth, R.E., 2015. An experimental investigation into the role of phyllosilicate content on earthquake propagation during seismic slip in carbonate faults. J Geophys Res-Sol Ea 120, 3187–3207. doi:10.1002/2015JB011914

Del Gaudio, P., Di Toro, G., Han, R., Hirose, T., Nielsen, S., Shimamoto, T., Cavallo, A., 2009. Frictional melting of peridotite and seismic slip. Journal of Geophysical Research 114, B06306–19. doi:10.1029/2008JB005990

Ferri, F., Di Toro, G., Hirose, T., Han, R., Noda, H., Shimamoto, T., Quaresimin, M., de Rossi, N., 2011. Low- to high-velocity frictional properties of the clay-rich gouges from the slipping zone of the 1963 Vaiont slide, northern Italy. Journal of Geophysical Research: Solid Earth (1978–2012) 116, B09208. doi:10.1029/2011JB008338

Hirono, T., Tsuda, K., Tanikawa, W., Ampuero, J.-P., Shibazaki, B., Kinoshita, M., Mori, J.J., 2016. Near-trench slip potential of megaquakes evaluated from fault properties and conditions. Sci. Rep. 1–13. doi:10.1038/srep28184

Houston, H., Benz, H.M., Vidale, J.E., 1998. Time functions of deep earthquakes from broadband and short-period stacks. J Geophys Res-Sol Ea 103, 29895–29913. doi:10.1038/ncomms3606

Jaeger, J.C., Cook, N., Zimmerman, R., 2007. Fundamentals of rock mechanics.

Ma, S., 2012. A self-consistent mechanism for slow dynamic deformation and tsunami generation for earthquakes in the shallow subduction zone. Geophys. Res. Lett 39, n/a–n/a. doi:10.1029/2012GL051854

Mitsui, Y., Yagi, Y., 2013. An interpretation of tsunami earthquake based on a simple dynamic model: Failure of shallow megathrust earthquake. Geophys. Res. Lett 40, 1523–1527. doi:10.1002/grl.50266

Mizoguchi, K., Hirose, T., Shimamoto, T., Fukuyama, E., 2009. High-velocity frictional behavior and microstructure evolution of fault gouge obtained from Nojima fault, southwest Japan. Tectonophysics 471, 285–296. doi:10.1016/j.tecto.2009.02.033

Proctor, B.P., Mitchell, T.M., Hirth, G., Goldsby, D., Zorzi, F., Platt, J.D., Di Toro, G., 2014. Dynamic weakening of serpentinite gouges and bare surfaces at seismic slip rates. J Geophys Res-Sol Ea 119, 8107–8131. doi:10.1002/2014JB011057

Tanioka, Y., Satake, K., 1996. Tsunami generation by horizontal displacement of ocean bottom. Geophys. Res. Lett 23, 861–864. doi:10.1029/96GL00736

Togo, T., Shimamoto, T., Ma, S., Hirose, T., 2011. High-velocity frictional behavior of Longmenshan fault gouge from Hongkou outcrop and its implications for dynamic weakening of fault during the 2008 Wenchuan earthquake. Earthq Sci

24, 267–281. doi:10.1007/s11589-011-0790-6
Yao, L., Ma, S., Shimamoto, T., Togo, T., 2013a. Structures and high-velocity frictional properties of the Pingxi fault zone in the Longmenshan fault system, Sichuan, China, activated during the 2008 Wenchuan earthquake. Tectonophysics 599, 135–156. doi:10.1016/j.tecto.2013.04.011
Yao, L., Shimamoto, T., Ma, S., Han, R., Mizoguchi, K., 2013b. Rapid postseismic strength recovery of Pingxi fault gouge from the Longmenshan fault system: Experiments and implications for the mechanisms of high-velocity weakening of faults. J Geophys Res-Sol Ea 118, 4547–4563. doi:10.1002/jgrb.50308